Coupling bimolecular PARylation biosensors with genetic screens to identify PARylation targets

Dragomir B. Krastev[1], Stephen J. Pettitt[1], James Campbell[1], Feifei Song[1], Barbara E. Tanos[2], Stoyno S. Stoynov[3], Alan Ashworth[1,4*], Christopher J. Lord[1*]

[1]The CRUK Gene Function Laboratory and Breast Cancer Now Toby Robins Research Centre, The Institute of Cancer Research, London, SW3 6JB, UK. [2]The Cancer Therapeutics Division, The Institute of Cancer Research, London, SW3 6JB, UK. [3]The Institute of Molecular Biology, Bulgarian Academy of Sciences, Sofia 1113, Bulgaria, [4]current address: The UCSF Helen Diller Family Comprehensive Cancer Center, 1450 3rd St, San Francisco, CA 94158, USA

*Correspondence to: Chris.Lord@icr.ac.uk, Alan.Ashworth@ucsf.edu

Keywords: PARylation, biosensor, tankyrase, transposon, genetic screen, centrosome

Abstract

Poly (ADP-ribose)ylation is a dynamic protein modification that regulates multiple cellular processes. Here, we describe a system for identifying and characterizing PARylation events that exploits the ability of a PBZ (PAR-binding zinc finger) protein domain to bind PAR with high-affinity. By linking PBZ domains to bimolecular fluorescent complementation biosensors, we developed fluorescent PAR biosensors that allow the detection of temporal and spatial PARylation events in live cells. Exploiting transposon-mediated recombination, we integrate the PAR biosensor *en masse* into thousands of protein coding genes in living cells. Using these PAR-biosensor "tagged" cells in a genetic screen we carry out a large-scale identification of PARylation targets. This identifies CTIF (CBP80/CBP20-dependent translation initiation factor) as a novel PARylation target of the tankyrase enzymes in the centrosomal region of cells, which plays a role in the distribution of the centrosomal satellites.

Introduction

Poly ADP-ribosylation (PARylation) is a highly dynamic and reversible post-translation protein modification that is generated by a family of PAR polymerases (PARPs, ARTDs). The PARP superfamily encompasses 17 proteins, of which only PARP1, 2 and tankyrases (TNKS and TNKS2, also known as PARP5a and 5b) display a clear PARP activity[1]. The remaining family members are mono ADP-ribose transferases or lack enzymatic activity. PARP1, 2 and 3 are nuclear proteins involved in DNA damage responses (DDR)[2], while tankyrases regulate a variety of cellular processes including telomere maintenance[3], Wnt signaling[4] and mitotic progression[5]. The role of PARP1, 2 and 3 in the DDR provided the rationale for the discovery and development of clinical PARP inhibitors. In addition, tankyrase inhibition can suppresses constitutive Wnt signaling[4], which has led to the discovery of a series of small molecule TNKS/TNKS2 inhibitors[7],[8]. Given the burgeoning interest in the PARP superfamily enzymes as drug targets and their role as mediators of cellular signaling processes, identifying and characterizing the targets of these enzymes is critical.

A number of studies have identified PARylation targets *en masse* by isolating proteins that bind to either anti-PAR antibodies or PAR-binding protein domains and identifying these by mass-spectrometry[9]. PARylation is often a transient modification, therefore some studies have used exposure to DNA damaging agents to enhance DNA damage-dependent PARylation, or suppression of PAR glycohydrase (PARG) to prevent PAR degradation[10]. An additional complication

of such studies is that PARylation is often induced on non-specific targets during *in vitro* cell lysis[9], [11]. Hence, additional approaches to detect and characterise PARylation targets are required.

In this study, we describe a system for identifying and characterizing PARylation events that exploits the ability of PBZ (PAR-binding zinc finger) domains to bind PAR with high-affinity. By linking PBZ domains to bimolecularfluorescent complementation biosensors, we developed fluorescent PAR biosensors that allow the detection and localisation of PARylation events in live cells. Finally, by exploiting transposon mediated recombination, we integrated these PAR biosensors *en masse* into thousands of protein coding genes in living cells. Using these PAR-biosensor "tagged" cells in a genetic screen facilitates the large-scale identification of PARylation targets. Using this approach, we show that CTIF (CBP80/CBP20-dependent translation initiation factor) is a target of PARylation by tankyrases at centrosomes and plays a role in the distribution of the centrosomal satellites.

Results

PAR-binding domains serve as high-affinity cellular biosensors

We aimed to develop a set of PAR-biosensors that could detect PARylation events in living cells. To do this, we exploited the PAR binding ability of PBZ (PAR-binding zinc finger) domains derived from either APLF (aprataxin PNK-like factor) or CHFR (checkpoint protein with FHA and RING domains) to bind PAR

with high affinity[12]. Although several other PAR-binding domains exist (such as macro and WWE domains), we selected PBZ domains for the development of biosensors for the following reasons: (i) their well-defined structure with the possibility to engineer precise point mutations that abolish PAR binding[12], and (ii) their intermediate PAR binding affinity (weaker compared to macrodomains), which allows reversible binding (this is confirmed below), thus minimising the possibility of artefactual PAR stabilisation and interference with endogenous PARylation dependent processes. We fused the coding sequence of the APLF or CHFR PBZ domain to that of green fluorescent protein (GFP), generating PAR biosensors (Fig. 1a; from here onwards PBZ refers to the APLF domain and CHFR-PBZ will be explicitly written when it is used). We then compared the ability of PAR biosensors to detect DNA damage-induced PAR, when compared to PAR immunodetection with a commonly used anti-PAR antibody (10H). To elicit DNA damage-induced PARylation, we exposed HeLa cells to H_2O_2;; to reduce PAR, we exposed cells to the PARP1/2 inhibitor olaparib. In untreated cells, cells exposed to H_2O_2, or cells exposed to olaparib (Fig. 1b), the antibody and the biosensor signals were correlated (Spearman's rank correlation, r_s = 0.48, 0.53 and 0.39 respectively) suggesting that the biosensor signal recapitulated the detection of PARylation shown by immunodetection (exemplary images are shown in Supplementary Fig. 1a).H_2O_2 exposure caused a close to two-fold increase in 10H PAR signal compared to the basal state, whilst olaparib treatment did not lead to any significant decrease in PAR signal (Fig. 1c), consistent with the notion that the 10H antibody predominately recognizes long

damage-induced PAR chains, but fails to detect endogenous PARylation. In contrast, the PAR biosensor revealed a broader dynamic range; H_2O_2 exposure caused an above five fold increase in the nuclear GFP intensity (Fig. 1c), whilst olaparib treatment led to a two fold decrease, resulting in a 12 fold difference between the absence and damage-induced PAR levels.

We also assessed the ability of a PAR biosensor to monitor temporal changes in PARylation. To do this, we used PBZ-mRuby2 biosensor alongside a PARP1-GFP expression construct; this allowed us to temporally co-monitor PARP1 and PAR localisation on UV microirradiated regions of cells. To eliminate any potential interference from endogenous PARP1, we carried out these experiments in *PARP1*$^{-/-}$ cells (Methods; Fig. 1d). Localised laser microirradiation led to a rapid localisation of PARP1 to the site of DNA damage (within 200 ms), followed 300 ms later by localisation of PAR at the same site (Fig. 1e). After 30-60s, both the PARP1-GFP and PBZ-mRuby2 signals were reduced in a co-ordinated fashion (Fig. 1f),likely reflecting reduction of PARP1 localisation and activity after the initial stages of DNA repair. The binding of the biosensor to the microirradiated site was rapid and reversible as shown by FRAP experiments (Supplementary Fig. 1c). To confirm the specificity of this effect, we used two mutant PARP1-GFP fusions Fig. 1g): a DNA-binding deficient mutant of PARP1 with mutations of residues 43 and 44 that disrupt the ZnF1 domain (PARP1-p.[43delM;44F>I] [13]); or PARP1 with an E988K mutation that impairs catalytic activity. The PBZ-mRuby2 sensor signal at microirradiated regions was entirely

dependent upon wild-type PARP1 (Fig. 1hE). Exposure of HeLa cells to the clinical PARP inhibitor talazoparib also abolished the PBZ-mRuby2 sensor signal (Fig. 1i). Importantly, in this experiment PARP1-GFP was expressed at endogenous levels from a bacterial artificial chromosome (BAC) showing that PARP1 overexpression does not alter the behavior of the biosensor. Furthermore, using HeLa cells without any additional PARP1 expression, we assessed the behavior of PBZ-mRuby2 and CHFR-PBZ-GFP (Supplementary Fig. 1b). Both biosensors showed identical kinetics, confirming that the observed results are due to the dynamics of PAR modification rather than the specificities of the PBZ domain used. Taken together, this data suggested that the PAR biosensors we developed exhibited high sensitivity and PAR-dependent behavior and could be used to dynamically monitor the amount of cellular PARylation.

Development and validation of bimolecular fluorescent complementation (BiFC) biosensors of PARylation

The identification of PARylation targets via biochemical purification is confounded by the artefactual loss and gain of PARylation events during cell lysis[9]. As the PAR biosensors described above provided the ability to detect PARylation events in living cells, rather than in cell lysates, we assessed whether we could modify these so that they could be used in genetic screens to identify novel PARylation targets. To do this, we needed to solve two issues: (i) to design PAR biosensor systems that monitored the PARylation state of specific proteins, rather than the total amount of cellular PAR; and (ii) to design PAR biosensors that could

stabilize what might otherwise be relatively transient PARylation events. With these issues in mind, we designed a bimolecular fluorescent complementation (BiFC, "split-GFP") approach, shown schematically in Fig. 2a. In BiFC approaches[14], two non-fluorescent halves of a GFP molecule are expressed as fusion proteins with two query proteins; for example, the C-terminus of Venus GFP (VC) is fused to a query protein and the N-terminus of Venus GFP (VN) is fused to the PBZ domain (Fig. 2a). Hence, this would allow us to detect PARylation events by reconstituting a functional GFP molecule, when the query protein is PARylated. One advantage of such a system would be that whilst the PARylated state of some proteins might have biochemical half-lives in the range of seconds to minutes[15,16], the half-life of Venus GFP, once formed by VC-VN complementation, is in the range of hours[14], potentially stabilizing these events.

To test this approach, we generated PBZ-VN and PBZ-VC biosensors. Simultaneous introduction of these probes into HeLa cells in in the absence of exogenous DNA damage generated a characteristic pattern of multiple GFP-positive nuclear foci (Fig. 2b). When used in isolation, neither PBZ-VN nor PBZ-VC generated a detectable GFP signal. This suggested that the BiFC approach, compared to PBZ-GFP, might provide a more sensitive approach to monitoring PARylation events *in situ*.

To assess the specificity of the BiFC approach, we generated sensors that contained four cysteine to alanine mutations within PBZ (equivalent to APLF amino acid positions p.C379A, C385A, C421A and C427A) known to abolish

PAR binding[12]; we termed these probes as PBZ-4A-VN, and PBZ-4A-VC. The introduction of these mutations abolished the formation of GFP-positive nuclear foci (Fig. 2b). Co-staining of the cells with a PAR-binding reagent (MABE1031, Millipore; Fig. 2b, red) showed that only the co-expression of the wild type PBZ probes led to PAR stabilization, while this was not the case for single probes or the PBZ-4A co-expression (quantification of this effect is shown in Fig. 2c). The split-GFP PBZ biosensor showed around 6-fold increase in PARylation, while a PARylation inducing treatment (10 min of 1 mM H_2O_2) showed 3-4 fold induction. Importantly, in all the subsequent experiments shown in Fig. 3, 4 and 5 to detect PARylation on target proteins, we express only one PBZ construct (typically PNZ-VN), which does not lead to PAR stabilization on its own.

We introduced these sensors into *PARP1*$^{-/-}$ CAL51 cells and found that the absence of PARP1 prevented the detection of both GFP-positive nuclear foci and localized microirradiation PAR/GFP signal (Fig. 2d,e). This observation was therefore consistent with the central role of PARP1 as a nuclear PARP enzyme associated with the response to DNA damage[17]. Consistent with this observation, we found that the PARP1/2 inhibitor olaparib reduced PBZ-VC + PBZ-VN nuclear foci, whilst a potent PARP5A/B (Tankyrase) inhibitor ICR-TNKS-001 (ref. 8) did not (Fig. 2d).

Microirradiation experiments demonstrated that PBZ-VC + PBZ-VN could also monitor the temporal increase and then decrease in PARylation associated with microirradiation (Fig. 2e). In this case, only the wild type PBZ constructs, transfected in PARP1 wild type cells, showed efficient recruitment, showing the

198 dependence of this on the presence of PARP1. We believe that the kinetics of
199 recruitment in these experiments reflect the properties of recruitment of the split-
200 GFP PBZ probes rather than *in situ* assembly of the GFP molecules. The
201 formation of a mature GFP fluorophore *in situ* of assembly is typically observed in
202 10 min (as discussed in Fig. 2f)[18], hence the signal detection in the range
203 seconds is likely a reflection of the recruitment of a fraction of pre-assembled
204 GFP molecules. ThePBZ-4A-VN + PBZ-4A-VC sensors did not detect this
205 dynamic PAR signal (Fig. 2e). In addition, the accumulation and dissipation of
206 PAR was also not detected when PBZ-VN+PBZ-VC sensors were used in
207 *PARP1*$^{-/-}$ cells, suggesting once more that this PAR signal was PARP1
208 dependent (Fig. 2e). These kinetics were identical to those observed with the
209 PBZ-GFP sensor (Fig. 1f) suggesting that the fusion into the BiFC does not alter
210 the recognition and recruitment to PARP1-mediated PARylation sites.
211
212 Using PBZ-VN+PBZ-VC sensors to detect the temporal response to PARP1/2
213 inhibitor exposure (talazoparib) GFP foci were found in the cytoplasm (Fig. 2f,
214 yellow arrows) but were less frequent in the nucleus; when talazoparib was
215 removed from the tissue culture media, nuclear GFP foci reformed within minutes
216 (Fig. 2f, red arrows), whilst the frequency and intensity of cytoplasmic PAR foci
217 was reduced. One explanation for this effect might be that the cytoplasmic GFP
218 foci represented non-PARP1/2 mediated PARylation events (by PARP enzymes
219 such as tankyrases, PARP4 and/or PARP10/14/16, which are not inhibited under
220 these conditions), while nuclear GFP foci represented PARP1/2 mediated

PARylation; upon the removal of talazoparib, there is a rapid shift of PARylation from being mostly cytoplasmic to mostly nuclear due to the reactivation of PARP1. It should be noted that the possibility that talazoparib induces cytoplasmic stress granules, which are enriched in PAR, cannot be excluded as an alternative explanation. The appearance of the nuclear foci coincides with the time of GFP fluorophore maturation *in situ* of the split-GFP assembly, which is around 10 min[18], and it is unlikely to be due to sensor diffusion as this is a rather fast process (as assessed in Supplementary Fig. 1c).

Lastly, we assessed whether the BiFC sensors could identify known PARylation events associated with PARP superfamily enzymes other than PARP1/2. To do this, we generated VC fused sensors for four "query" protein PARylation targets of Tankyrase (PARP5A/B, TNKS/TNKS2): AXIN[4]; TERF1 (aka TRF1)[3]; TNKS2 itself (amino acids 800-1161, encompassing the SAM and CAT domains of the protein)[4]; and GLUT4[19]. These query protein-VC sensors were introduced into HeLa cells alongside either PBZ-VN or PBZ-4A-VN (Fig. 2g). In each case, combining the PBZ-VN sensor with a query protein-VC revealed a detectable fluorescent signal that had the expected cellular localization pattern (cytoplasmic degradosomes for AXIN and TNKS2, nuclear for TERF1, perinuclear and Golgi-like for GLUT4, Fig. 2f). In contrast, the PBZ-4A-VN biosensor generated only a marginally detectable fluorescent signal. We validated these signal by immunostaining with antibodies recognizing the endogenously expressed proteins (TERF1 and GLUT4 shown in Supplementary Fig. 2b,c), which revealed

partial or complete overlap of both signals. This suggests that the biosensor recognizes, *in situ*, only the PARylated fraction of the protein. It is particularly clear in the case of TERF1 (Supplementary Fig. 2b), which the antibody recognized throughout the nucleoplasm with some enrichment at the telomeres, while the biosensor signal is predominantly telomeric, which is where TRF1 is being PARylated[3]. Furthermore, CHFR-PBZ-VN biosensor showed virtually identical pattern to PBZ-VN, strengthening these observations.

Taken together, we concluded that these BiFC sensors demonstrated sufficient specificity for the PARylation state of a series of proteins and could be used to identify novel PARylation targets *in situ*, as described below.

A BiFC based genetic screen identifies novel PARylation targets

Using the BiFC sensors, we designed a genetic screening system aimed at identifying novel PARylation targets. The screening approach involved (Fig. 3a): (i) generating cellular libraries where each cell contained a VC coding sequence integrated into an endogenous gene by the use of a gene trap transposon[20]; (ii) introducing a PBZ-VN sensor into this cell library; (iii) selecting cells with VC-VN detectable PARylation events by FACS GFP-positive cells; and (iv) identifying the VC-containing gene by deep sequencing of genomic DNA flanking the transposon.

We relied upon the ability to integrate an in-frame VC coding sequence into multiple endogenous genes in any given cell population. This generated a population of cells where the expression of query gene-VC fusion was largely

267 controlled by the native promoter and enhancer DNA sequences, rather than
268 driving the transcription of query protein-VC fusions from a plasmid-based cDNA.
269 Gene trap transposons provide an effective way of generating such gene fusion
270 events within endogenous genes and so we adapted a Tol2-based UPATrap
271 vector to encompass a VC-coding sequence (a schematic of how the gene
272 trapping events occur is shown on Fig. 3b). Because Tol2 is a sequence-
273 independent cut-and-paste transposon[21], only one of the two alleles of a gene is
274 likely to be trapped, which implies that there would not be detrimental cellular
275 effects because of the second allele. We used the previously published
276 UPATrap[21], which contains two functional DNA cassettes: (i) at the 5′-end, a
277 promoterless splice acceptor (SA)-IRES-GFP-polyA sequence; and (ii) at the 3′-
278 end, a promoter-driven *NeoR* (G418 resistance) coding gene with a 3′ splice
279 donor sequence (*SD*). We modified UPATrap in three significant ways to allow
280 the generation of protein fragments fused to VC: (Supplementary Fig. 3a): (1) by
281 replacing the IRES-GFP sequences with a VC-coding sequence, generating a
282 SA-VC-polyA cassette; (2) by generating three different open reading frames of
283 the resultant transposon (UPATrap-VC 1, 2 and 3); and (3) by removing the IRES
284 sequence in the *NeoR* cassette. Removing the IRES, which suppresses the
285 nonsense mediated decay of fusion transcripts, biases the selection of resistance
286 towards the integration of the transposon in the 3’ of the captured genes (see
287 Methods).
288

To validate the gene trap ability of these modified transposons, we also generated an UPATrap-GFP version (full-length GFP in place of the VC), andcotransfected this with transposase-expressing plasmid into both HeLa and CAL51 tumour cells. After neomycin selection, we found that 19% of CAL51 neomycin-resistant (Neo^r) clones and 43% of HeLa Neo^r clones were GFP-positive. By isolating individual colonies from GFP-positive CAL51 cells, we found that each colony exhibited a different localization of the GFP signal (Fig. 3c), suggesting that the transposon had trapped different genes in each case. On the basis of these successful validation experiments, we generated gene trapped CAL51 cell libraries (i.e. populations of cells with the gene trap in different genes in different cells) using UPATrap-VC 1, 2 and 3 (Fig. 3a, b). We selected CAL51 cells in this instance as these cells have a diploid genome and an absence of large-scale genomic rearrangements. Ten million cells were electroporated with transposase plasmid and UPATrap-VC 1, 2 and 3 using a limiting dilution of transposon DNA to maximize the likelihood of a single transposon integration event per cell (Supplementary Fig. 3b, c, d)[22], generating ~50,000 gene-trapping events after neomycin selection. We divided this library into six sub-libraries and then transfected each sub-library with either PBZ-GFP, PBZ-VN or PBZ-4A-VN sensors (Fig. 3a (ii)). The PBZ-GFP construct shows the efficiency of the electroporation, which was typically in the range of 60-65% (Supplementary Fig. 3e). After culturing cells for 48 hours, GFP-positive cells were isolated by FACS (Fig. 3a (iii)). Compared to PBZ-GFP, introduction of PBZ-VN caused < 0.1% of cells to become GFP-positive, as expected for a probe only detecting VC tagged

PARylated proteins. After isolating genomic DNA (gDNA) from GFP-positive cells, we identified gene targeting events using an optimized non-restrictive linear amplification PCR method (nrLAM-PCR)[23]. This method amplifies the genomic region adjacent to each UPATrap-VC transposon insertion site, which was then sequenced using Ion Torrent sequencing. This PCR method was specific, as PCR products were only obtained from UPATrap-VC transposed cells and not from non-transposed cells (Supplementary Fig. 3f, g). We developed apipeline to align and annotate the sequenced reads as a means to identify UPATrap-VC insertion sites (see Methods). Each gDNA was amplified and sequenced in triplicate, resulting in a highly specific pattern of distribution of the sequencing reads (Supplementary Fig. 3h, i). We found that the number of unique DNA reads generated by triplicate amplification/sequencing procedures for each UPATrap-VC insertion site to be highly correlated (Spearman's correlation r_s>0.98, Fig. 3d). In total, we identified 400 UPATrap-VC insertion sites in the GFP-positive cells; 50 of these genomic sites were represented with a high number of unique reads (>30 reads/site), with the rest forming a long-tail distribution in terms of read depth (Fig. 3e). From these 50, we filtered out genomic loci identified in the PBZ-4A-VN screening arm as likely false positives, as well as those UPATrap-VC insertion sites unlikely to form genuine gene-VC e.g. those integrations in gene deserts. The remaining 20 UPATrap-VC insertion sites were located in 17 genes, with three genes showing two independent integration events: *NPM1* (Nucleophosmin, B23), *CTIF* (Cap binding complex dependent translation initiation factor) and CCDC171 (Coiled-coil domain containing 171) (Fig. 3f and

Table 1). Given the low transposon/cell number ratio used, these multiple insertion events in *NPM1*, *CTIF* and *CCDC171* originated in different cells and therefore represented independently occurring events. Due to the complexity of the screen, and to the depth of sequencing that can be achieved with the nrLAM-PCR, we believe that the screen was conducted in under-saturating conditions. It is likely that we show a sampling of the PARylome and that further iterations of the screen would be necessary to achieve saturation.

One of these three genes identified by independent integration events, *NPM1*, encodes a known PARylated protein that resides, together with PARP1/2, in the nucleoli of cells[24,25,9]. We found that the NPM1-VC + PBZ-VN GFP signal had a precise nucleolar localization, which partially coincided with endogenous NPM1 as shown by antibody staining (Fig. 3g). The identification of this *bona fide* PARylated protein gave us confidence that we have identified genuine PARylation targets in the screen. We also generated VC sensors for an additional 10 candidate PARylated target proteins and examined the cellular localization with the PBZ-VN. In each case, we observed a specific subcellular localization pattern (Fig. 3h). We validated these localisation patterns in the case of CTIF (Fig. 3g and the rest of this study) and ILF3 (Supplementary Fig. 2d) by antibody co-staining, which showed partial overlap with between the protein and the biosensor. It is important to point out that we have attempted to co-localise the biosensor signal for a subset of these genes with a staining with PAR-binding reagent (Millipore). As shown in Supplementary Fig. 2d, in five examined cases we failed to observe co-staining (with an exception of CTIF where a mild co-

localisation is observed; this point is addressed below). Crucially, two of these proteins (TERF1 and GLUT4) are validated PARylation targets, which this staining failed to confirm. This shows that staining with the PAR reagent is not a reliable way to validate targets, and that the biosensor has the potential to achieve higher sensitivity.

We chose to further characterise CTIF as it was identified with multiple transposon integration sites and its biosensor exhibited a specific, perinuclear localization (Fig. 3g and Fig. 4).

CTIF is a TNKS-dependent PARylation target

We identified two independent integration sites in the last two introns of the *CTIF* gene, generating two C-terminal truncations as shown in Fig. 4a,b,c. Other than its role in CBP80/20-dependent translation and nonsense mediated RNA decay[26], very little is understood about the function of CTIF. Examination of the CTIF-VC+PBZ-VN (or CHFR-PBZ-VN) sensor signal suggested that CTIF PARylation was localized to a cluster of peri-nuclear granules (Fig. 4d). Importantly, this localisation was not observed when PBZ-4A-VN sensor was used (Supplementary Fig. 4a). The expression of a VN-only fragment, showed a diffuse cytoplasmic localization (Supplementary Fig. 4a), similar to a full-length CTIF-GFP sensor (Fig. 4e), suggesting that CTIF was also localized to the cytoplasm, similar to previous observations[26]. However, PARylation of CTIF, as detected by CTIF-VC+PBZ-VN sensors, occurred predominantly in the centrosomal area of the cell (Fig. 4e). We validated the centrosomal location by

the expression of centrosomal markers (CETN2-GFP or Cep170-GFP) or staining for centrosomal markers (CETN3 and gamma-Tubulin) (Fig. 4e). Interestingly, endogenous CTIF showed enrichment only at the daughter centriole – it co-localises with one of the CETN2-GFP marked centrioles, but is completely excluded from the mother centriole, marked by Cep170-GFP (Fig. 4e, F and Supplementary Fig. 4c). This shows that CTIF has a *bona fide* centrosome targeting. This is further substantiated by CTIF-GFP, which shows a broad cytoplasmic distribution with enrichment at the centrosome (Fig. 4e). In contrast, CTIF-VC+PBZ-VN biosensor shows strong centrosomal enrichment in an area surrounding the centrosomal markers used (Fig. 4e).

One of the transposon insertions in *CTIF* was predicted to fuse VC to a truncated CTIF protein comprising the N-terminal 511 out of the 600 amino acids of the full-length protein (CTIF 1-511). We generated a CTIF 1-511-VC sensor, which when combined with PBZ-VN, generated an identical GFP localisation pattern to full-length CTIF-VC+PBZ-VN (Supplementary Fig. 4b). In order to identify which PARP superfamily member is responsible for the CTIF biosensor behavior, we exposed cells to either olaparib (a PARP1/2 inhibitor) or ICR-TNKS-001 (a tankyrase inhibitor[8]), and assessed the CTIF-VC+PBZ-VN signal. Whilst the signal was unaffected by olaparib exposure, its intensity and cellular distribution was largely suppressed by the tankyrase inhibitor (Fig. 4g). Tankyrase inhibition did not abolish the ability of CTIF to bind to the centrosome (Supplementary Fig. 4c), but rather abolished the formation of the biosensor signal in the broader area

surrounding the centrioles. Furthermore, RNA interference-mediated silencing of *TNKS* and *TNKS2* led to decreased CTIF-VC+PBZ-VN biosensor signal without affecting the total CTIF level (Fig. 4h,i). CTIF-GFP immunoprecipitation revealed that CTIF is directly PARylated, and that this PARylation was suppressed by tankyrase inhibition (Fig. 4j and Supplementary Fig. 4f). Probing the same blots for the presence of tankyrase failed to identify an interaction. Tankyrase binds its targets by recognising a canonical motif[27]. By this definition CTIF posses two motifs in its N-terminal domain, albeit with a suboptimal sequence (lacking the critical arginine residue at position +1) (Supplementary Fig. 4d). We generated a CTIF mutant with the critical amino acids at the +1 and +6 positions in each motif replaced by alanine and assessed its cellular localisation; no significant change in the intensity or localisation of the biosensor signal of the mutant was observed when compared to wild type CTIF (Supplementary Fig. 4e), suggesting that these two motifs are not genuine tankyrase recognition sequences. Yet, by generating an allelic series of CTIF-VC sensors with different CTIF deletion events, we found that the N-terminal 100 amino acids of CTIF were sufficient for the localization of CTIF-VC+PBZ-VN to the centrosome, while the C-terminal domain interacts with a pool of cytoplasmic granules (Fig. 4k and Supplementary Fig. 4g). Taken together, these data suggested that CTIF is a direct target of tankyrase-mediated PARylation, but its recognition may be mediated through interactions with another proteins, potentially located in the N-terminal portion of the protein.

CTIF affects the distribution of centrosomal satellites

To understand the nature of CTIF PARylation, we exploited the ability of a PAR biosensor to monitor the temporal and subcellular localisation changes in the passage of a cell cycle. We introduced CTIF-VC+PBZ-VN or CTIF-GFP biosensors into H2B-Cherry expressing HeLa cells and imaged them over one cell cycle (Fig. 5a). Whilst CTIF-GFP showed a largely homogeneous cytoplasmic distribution throughout the cell cycle, the CTIF-VC+PBZ-VN GFP signal was clustered in granular structures around the centrosome during interphase (Fig. 5a). As cells progressed towards mitosis the biosensor intensity increased and coalesced at the centrosome in G2 (Supplementary Fig. 5a); in mitosis the signal clearly segregated along with the two centrosomes. These granular structures were transported towards the centrosome in a microtubule-dependent manner as exposure of cells to the microtubule depolymerizing agent (nocodazole) led to their reversible cytoplasmic dispersal; a microtubule stabilizing agent (paclitaxel) had no such effect (Fig. 5b).

Tankyrase is a known regulator of centrosome behavior[5,28], and our data suggested that it PARylaes CTIF. The dynamic pattern of CTIF PARylation was reminiscent of the behavior of the centrosomal satellites[29,30]. This prompted us to further investigate localization of the CTIF biosensors with respect to various additional centrosomal markers (Fig. 5c). We found that the CTIF-VC+PBZ-VN surrounded the inner centrosomal markers CETN2, CETN3, PCNT and gamma-tubulin (Fig. 4e and Fig.. 5d). It also occupied the centrosomal area together with various centrosomal satellite markers (PCM1, Cep131/Azi1, Cep290 and BBS4,

Fig. 5d), although not co-localizing with them. Tankyrase co-localised with the CTIF-VC+PBZ-VN biosensor signal (Fig. 5e), supporting our previous data that suggested that CTIF might be a tankyrase target protein.

To investigate the functional effect CTIF might have on centrosomal proteins, we depleted CTIF by RNA interference (RNAi). Whilst *CTIF* RNAi did not obviously influence the localisation of inner centrosomal markers (e.g. PCNT, Fig. 5f,h),certain centrosomal satellite proteins (Cep131/Azi1, Cep290 and BBS4) became less localized (quantification for Cep131/Azi1 is shown in Fig. 5f,g). Interestingly, other satellite markers (e.g. PCM1 and OFD1) seemed unaffected (Supplementary Fig. 5b; phenotypes are summarized in Table 2). Tankyrase depletion had a similar, although less pronounced effect, upon the same subset of markers (Fig. 5f,g). Taken together with our earlier observations, this data suggested that CTIF PARylation, most likely via tankyrases, is associated with centrosomes, and that this tankyrase-CTIF axis might play a role in the localisation or recruitment of centrosomal satellite proteins.

Discussion

In this study, we describe a biosensor-based approach to identify PARylation events and targets. The system we describe possesses several advantageous qualities. The ability to detect PARylation without the requirement to lyse cells facilitates the detection of steady state PARylation in living cells but also temporal and spatial changes in PARylation. These sensors can be integrated into a genetic screening systems, including the transposon-based system described here, enabling the detection of novel PARylation related events. Our data suggest that CTIF is PARylated in the proximity of the centrosome in a tankyrase-dependent manner..Subsequent work is necessary to investigate CTIF's precise role at the centrosome. Intriguingly, CTIF localises to the growing daughter centriole where localized RNA translation could be associated with the translation of a subset of necessary proteins,, similarly to what was previously shown in the case of OFD1 (ref. 31).

There will be caveats associated with the PAR-biosensors e.g. protein tagging that may alter normal cellular behavior. Importantly,although we have not observed gross aggregation of tagged proteins a major concern remains the level of tagged protein expression, which may cause artefactual phenotypes in the biosensor system. There exists the possibility that the PAR-binding may stabilise PARylation events to some extent. This is advantageous in terms of detecting transient PARylation events, but might also be problematic if it interferes with

normal molecular processes. In each case, the observed phenotypes need to be validated by orthogonal methods.

Other methods of gene perturbation e.g. CRISPR-Cas9 mediated gene tagging (e.g. CRISPaint[32]) or gene mutagenesis (e.g. CRISPR tiling arrays[13]) could be integrated intoexperimental workflows that use PAR biosensors. The PBZ-based biosensors recognise a specific aspect of the PAR chains (the α(1-2) O-glycosidic bond between the ADP-ribose units); other PAR binding domains (e.g. macrodomains or WWE motifs) recognise different aspects of the PAR chain[33]. We envisage that a range of biosensors can be created that report on different facets of PAR biology. Finally, PAR biosensors could be adapted to capture PARylation events in live animals, which lead to better understanding of the effects of PARP inhibitors in different tissues *in vivo*..

Methods

Cells

CAL51 and HeLa cells were grown in DMEM (Gibco) supplemented with 10% FBS, penicillin-streptomycin (ThermoFisher). CAL51 *PARP1*$^{-/-}$ cells were generated by GE Dharmacon Edit-R Gene Engineering System, by transfecting with 1 µg Edit-R CRISPR-Cas9 Nuclease Expression Plasmid mixed with 2.5 µl of 20 µM *PARP1* crRNA (GAC CAC GAC ACC CAA CCG GAG UUU UAG AGC UAU GCU GUU UUG,) and 2.5 µl of tracrRNA (20 uM), using Lipofectamine 3000 reagent according to the manufacturer's instructions (Life Technologies). Three days post transfection, cells were selected in 100 nM talazoparib for five days, and surviving cells were FACS sorted to isolate single clones. Biallelic genome modification was confirmed by Sanger sequencing. HeLa cells expressing PARP1-LAP construct have been previously described[34].

Constructs

The PAR biosensors are based on the APLF amino acids 371-451 or CHFR amino acids 407-665 sequence respectively, which were synthesized and cloned into pEGFP-N1 (Clontech), the EcoRI/KpnI site of pBiFC-VN173 (Addgene #22010) and pBiFC-VC155 (Addgene #22011, ref. 35), and pcDNA3-mRuby2 (Addgene #40260, ref 36). In the APLF-based biosensor, Cys-to-Ala mutations were introduced in C379, C385, C421 and C427 to generate the 4A versions of the above constructs. Full-length FLAG-PARP1 was cloned in pEGFP-N1 vector. DNA-binding deficient (p.delM43F44I[13]) and catalytic-deficient mutant (E988K)

were introduced with site-directed mutagenesis. Hits identified in the PARylation screen were amplified from a cDNA library and cloned in the pBiFC-VC155 vector. Full-length *CTIF* was amplified from a cDNA library and cloned in pEGFP-N1 or pBiFC-VC155 vector. CTIFm2 mutant, carrying the following substitutions – K44A, G49A, L150A and G155A, was produced by gene synthesis and cloned into the pBiFC-VC155 vector. UPATrap-VC/GFP vectors are based on the UPATrap technology[21]. The IRES-GFP moiety of UPATrap-Tmat vectors 1, 2 and 8 (Genbank accession numbers AB673346, AB673347, AB673353) was replaced by HA-VC155 or HA-EGFP; the HA sequence starts 15 base pairs downstream of the SA and lacks an ATG codon. To cover the three possible reading frames, three vectors were created, which have 0, 1 or 2 C bases in front of the HA sequence. The IRES from the splice donor (SD) cassette was excised in order to bias the selection of integration sites towards the last introns. CETN2-GFP (#41147) and Cep170-GFP (#41150) expressing constructs were acquired from Addgene.

Antibodies

GFP (Roche, 11814460001; 1:2000), PAR 10H (Trevigen, 4335-AMC-050; 1:200), PAR binder (Millipore, MABE1031, 1:1000), CTIF (Sigma-Aldrich, HPA016865-100UL; 1:1000), TERF1 (Abcam, ab10579; 1:1000), GLUT4 (Abcam, ab654; 1:1000), ILF3 (Abcam, ab92355; 1:1000), NPM1 (Abcam, ab10530; 1:1000), CETN3 (Abnova, H00001070-M01; 1:500), PCNT (Atlas antibodies, HPA016820; 1:500), PCM1 (Cambridge bioscience, A301-149A; 1:500), gamma-

tubulin (Sigma-Aldrich, T6557-100UL; 1:500), Azi1/Cep131 (Abcam, ab84864; 1:500), Cep290 (Abcam, ab84870; 1:500), BBS4 (Proteintech, 12766-1-AP; 1:500), OFD1 (Proteintech, 22851-1-AP; 1:500), TNKS1/2 (Santa Cruz, sc-8337; 1:1000), alpha-tubulin (Sigma-Aldrich, T9026; 1:10000), beta-actin (Sigma-Aldrich, A1978; 1:10000).

Reagents

Olaparib (Selleckchem), ICR-TNKS-001 (ref. 8), Nocodazole (Sigma, M1404-10MG), Paclitaxel, H_2O_2 (Sigma, 216763-100ML), G418 (Sigma, G8168-100ML).

siRNA

The following siRNAs were provided by GE Healthcare *siCTIF* (M-021020-01-0005), *siTNKS* (M-004740-01-0005), *siTNKS2* (M-004741-01-0005).

Transfection

DNA constructs were transfected with Lipofectamine 2000 (Life Technologies) according to manufacturer instructions. Typically, for a 24-well plate a mix of 175 ng of gene-VC and 25 ng sensor-VN was transfected. For siRNA transfection Lipofectamine RNAiMax was used (Life Technologies) according to manufacturer instructions.

Immunoprecipitation and western blotting

Immunoprecipitation was typically carried out from close-to-confluence 10-cm dishes transfected in advance with appropriate construct. Cells were washed with PBS, collected and lysed in Net-N buffer (50 mM TrisHCl pH7.5, 1 mM EDTA, 0.5% IGEPAL CA-630, 1 mM DTT, protease inhibitors (Sigma, cOmplete mini), sonicated and cleared by centrifugation. 0.5-1 mg total protein extract was incubated with GFP_Trap beads (Chromotek) for 1 hour at 4°C with rotation. Beads were washed five times with lysate buffer and proteins were eluted by heat denaturation in loading dye. Samples were resolved on NuPAGE protein gels (ThermoFisher), transferred to nitrocellulose membrane and blocked in 5% milk. Anti-PAR (1:2000) and anti-GFP (1:2000) were incubated at 4°C overnight. Proteins were detected and quantified on the Odyssey Fc imaging system (LiCor).

Cellular libraries construction and screening

$1x10^7$ CAL51 cells were electroporated with 30 ng UPATrap-VC (each open reading frame) and 1400 ng Tol2 transposase expressing plasmid. They were split and kept as six independent cellular libraries. The cells were selected with 0.8 mg/ml G418 for 10 days. Colony formation assay showed that each cellular library contained ~5000 independent clones. Libraries were expanded to a representation of 1000 cell/clone and frozen down. For the PARylation screen, each library was divided into three identical aliquots (each aliquot had $5x10^6$ cells, to ensure ~1000 cells representation for each of the 5,000 VC-gene trap events). The first aliquot was electroporated with a wild type (PBZ-GFP) biosensor expression plasmid to monitor the efficiency of electroporation, which was 60%.

The second aliquot was electroporated with a wild type (PBZ-VN) biosensor expression plasmid and the third aliquot was electroporated with a mutant (PBZ-4A-VN) VN linked biosensor. After 48 hours, the GFP-positive fraction from the PBZ-VN and PBZ-4A-VN aliquots (<0.1 % of each library) was isolated by FACS. These cells were expanded and aliquots were frozen and gDNA prepared (Blood and Tissue kit, Qiagen).

nrLAM protocol

nrLAM-PCR protocol was adapted and optimized from ref. 23 as follows. For each gDNA sample three independent reactions were run. 50 µl reactions, containing 1.25 U Taq (NEB), 1 µg gDNA, 0.5 µl 0.17 µM biotin-SPL1 primer and 2 µl 0.5 mM dNTPs, were cycled – 95°C/2', 50x(95°C/45", 58°C/45", 72°C/10"). After one run, 1.25 U Taq was added and the PCR program repeated. Biotinylated products were collected on streptavidin beads (Life Technologies 11205D), washed and re-suspended in a ligation mastermix, containing 25% w/v PEG8000 (Sigma 89510-250G-F), 1 µM ssAdapter, 1 mM $Co(NH_2)_6Cl_3$ (Sigma H7891-5G), 1x T4 ligation buffer and 20 U T4 ligase (NEB), for 16 h at 25°C and 300 rpm shaking. Reactions were diluted with 90 µl water, beads were collected and washed with 100 µl water. Finally they were re-suspended in 25 µl water and 5 µl were used in a 50 µl Q5 (NEB) PCR reaction with 0.2 µM SPL-1 and 0.2 µM HmSp1 primers - 98°C/30", 20x(98°C/20", 70°C/20", 72°C/1'), 72°C/2'. 1 µl of this PCR reaction was used as a template in a subsequent reaction: 50 µl Q5 PCR reaction with 0.2 µM P1trunc and 0.2 µM IonTorrent_index primers - 98°C/30",

10x(98°C/10”, 61°C/10”, 72°C/1’), 10x(98°C/10”, 69°C/10”, 72°C/1’), 72°C/2’. PCR products were obtained only from Tol2-containing gDNA. DNA libraries were purified with a PCR purification kit (Qiagen) and sequenced on Ion Torrent PGM 318 chip, 400 flow.

Biotin-SPL1 – 5′CATGCATCATATCCATCGCAATCGCATCC

ssAdapter – 5’ GATCACCGACTGCCCATAGAGAGGGGTCTCTCCTAGCAACGGTTACTCTTCG (NB: 5′-P, phosphorthioate last C-G bond, 3′-C3 blocking group)

SPL-1 – 5′CATGCATCATATCCATCGCAATCGCATCC

HmSp1 – 5′CGAAGAGTAACCGTTGCTAGGAGAGACC

P1trunc – 5′CCTCTCTATGGGCAGTCGGTGATC

AdapterindexTol2- 5′CCATCTCATCCCTGCGTGTCTCCGACTCAGN_{10}GATTTTGAGTACTTTTTACACCTCTG

Data analysis

The data analysis pipeline is online in a diagram in Supplementary Fig. 6. Briefly, fastq files were obtained from Ion Torrent sequencing. The Tol2 sequence (5′TTTGAGTACTTTTTACACCTCTG) was removed from all the reads by cutadapt-1.4.2 and they were further aligned to the human genome GRCh37, using bwa-0.7.9a[37]. From the alignment bam/bed files were generated. Using bedtools[38] master blocks were generated, covering the coordinates of any overlapping bed across all sequenced samples. PCR duplicates were removed

644 from the bed files and only unique-length reads were counted. Each bed file was
645 intersected with the master block and with gene annotation bed files. In this way,
646 one generates a unique integration site identifier (master block) for which unique
647 reads can be counted for each sample. Finally, the unique-length read count
648 information was intersected across samples. This generated the initial hit list of
649 integration sites with their counts.
650 The initial hit list was subjected to the following filtering criteria. Firstly, integration
651 sites with less than three unique-length reads were discarded. Secondly, every
652 authentic integration site should produce a stacked pyramidal arrangement of
653 reads that have to be co-oriented with the direction of transcription of the host
654 gene e.g. Supplementary Fig. 3h,i. Hence, anti-oriented sites were discarded.
655 The sites in the resulting list were further filtered based on the following criteria:
656 discarded were sites found in the negative control (PBZ-4A-VN sensor), sites
657 located outside of known genes and sites whose splicing would not lead to the
658 expression of gene-VC fusion (based on the precise location of the integration
659 site within a gene). Furthermore, genes with multiple independently identified
660 integration sites were noted as high-confidence hits.
661
662 **Imaging and microirradiation**
663 Cells were seeded on coverslips and transfected with biosensor constructs. After
664 48 hours incubation, the cells were fixed with 1% PFA solution at room
665 temperature for 10 min. Cells were permeabilized with 0.2% Triton X-100 in PBS
666 and blocked with IFF (2% BSA, 1% FBS in PBS). Antibody incubation was

carried out in IFF with primary antibody typically in 1:500 dilution; secondary antibody (alexa594-conjugated, ThermoFisher) was used in 1:1000 dilution. Cover slips were mounted on ProLong Gold Antifade (ThermoFisher) and imaged on a Zeiss LSM 780 confocal microscope.

For microirradiation, cells were grown in glass-bottom culture dishes (MaTek, P35G-0.170-14-C) and transfected with required constructs. 24 hours post transfection imaging was done on Andor Revolution system, 60x water objective with micropoint at 365 nm. Measured were only cell with similar intensity of the GFP signal. The background intensity (in the vicinity of the microirradiation area in the nucleus) was subtracted from that at the microirradiation point and the maximum was normalised to 1. For the FRAP experiments the same system was used with the following FRAPPA settings – dwell time – 60, repeat – 10 and laser intensity – 6%.

Data availability

The constructs used in this study are available upon request to the authors or at Addgene (https://www.addgene.org/Chris_Lord/, Plasmid IDs #110646-110653). Transposon integration site sequencing data has been deposited at the European Nucleotide Archive with study number PRJEB26343.

Acknowledgements

We would like to express our gratitude to Dr. Yoon Ki Kim's laboratory for sharing reagents. This work was funded by Breast Cancer Now (BBC070X) and Cancer Research UK through Programme Grants (CRM059X) to CJL.

Author contributions

DBK, AA and CJL designed the study and wrote the manuscript. DBK and SJP conducted experiments, JC conducted bioinformatics analysis, FS generated CAL51 *PARP1*$^{-/-}$ cell line, BET assisted the centrosome analysis, SSS conducted imaging and microirradiation studies. AA and CJL supervised the study.

Conflict of interests

The authors declare no competing interests.

References

1. Vyas, S. et al. Family-wide analysis of poly(ADP-ribose) polymerase activity. *Nat Commun* **5**, 4426 (2014).
2. Gibson, B.A. & Kraus, W.L. New insights into the molecular and cellular functions of poly(ADP-ribose) and PARPs. *Nat Rev Mol Cell Biol* **13**, 411-424 (2012).
3. Smith, S., Giriat, I., Schmitt, A. & de Lange, T. Tankyrase, a poly(ADP-ribose) polymerase at human telomeres. *Science* **282**, 1484-1487 (1998).
4. Huang, S.M. et al. Tankyrase inhibition stabilizes axin and antagonizes Wnt signalling. *Nature* **461**, 614-620 (2009).
5. Chang, P., Coughlin, M. & Mitchison, T.J. Tankyrase-1 polymerization of poly(ADP-ribose) is required for spindle structure and function. *Nat Cell Biol* **7**, 1133-1139 (2005).
6. Lord, C.J. & Ashworth, A. PARP inhibitors: Synthetic lethality in the clinic. *Science* **355**, 1152-1158 (2017).
7. Riffell, J.L., Lord, C.J. & Ashworth, A. Tankyrase-targeted therapeutics: expanding opportunities in the PARP family. *Nat Rev Drug Discov* **11**, 923-936 (2012).
8. Elliott, R.J.R. et al. Design and discovery of 3-aryl-5-substituted-isoquinolin-1-ones as potent tankyrase inhibitors. *MedChemComm* **6**, 1687-1692 (2015).

9. Jungmichel, S. et al. Proteome-wide identification of poly(ADP-Ribosyl)ation targets in different genotoxic stress responses. *Mol Cell* **52**, 272-285 (2013).
10. Zhang, Y., Wang, J., Ding, M. & Yu, Y. Site-specific characterization of the Asp- and Glu-ADP-ribosylated proteome. *Nat Methods* **10**, 981-984 (2013).
11. Beneke, S., Meyer, K., Holtz, A., Huttner, K. & Burkle, A. Chromatin composition is changed by poly(ADP-ribosyl)ation during chromatin immunoprecipitation. *PLoS One* **7**, e32914 (2012).
12. Ahel, I. et al. Poly(ADP-ribose)-binding zinc finger motifs in DNA repair/checkpoint proteins. *Nature* **451**, 81-85 (2008).
13. Pettitt, S.J. et al. Genome-wide and high-density CRISPR-Cas9 screens identify point mutations in PARP1 causing PARP inhibitor resistance. *bioRxiv* (2017).
14. Hu, C.D., Chinenov, Y. & Kerppola, T.K. Visualization of interactions among bZIP and Rel family proteins in living cells using bimolecular fluorescence complementation. *Mol Cell* **9**, 789-798 (2002).
15. Alvarez-Gonzalez, R. & Althaus, F.R. Poly(ADP-ribose) catabolism in mammalian cells exposed to DNA-damaging agents. *Mutat Res* **218**, 67-74 (1989).
16. Malanga, M. & Althaus, F.R. Poly(ADP-ribose) molecules formed during DNA repair in vivo. *J Biol Chem* **269**, 17691-17696 (1994).
17. Ray Chaudhuri, A. & Nussenzweig, A. The multifaceted roles of PARP1 in DNA repair and chromatin remodelling. *Nat Rev Mol Cell Biol* **18**, 610-621 (2017).
18. Robida, A.M. & Kerppola, T.K. Bimolecular fluorescence complementation analysis of inducible protein interactions: effects of factors affecting protein folding on fluorescent protein fragment association. *J Mol Biol* **394**, 391-409 (2009).
19. Chi, N.W. & Lodish, H.F. Tankyrase is a golgi-associated mitogen-activated protein kinase substrate that interacts with IRAP in GLUT4 vesicles. *J Biol Chem* **275**, 38437-38444 (2000).
20. Kawakami, K., Shima, A. & Kawakami, N. Identification of a functional transposase of the Tol2 element, an Ac-like element from the Japanese medaka fish, and its transposition in the zebrafish germ lineage. *Proc Natl Acad Sci U S A* **97**, 11403-11408 (2000).
21. Mayasari, N.I. et al. Mixture of differentially tagged Tol2 transposons accelerates conditional disruption of a broad spectrum of genes in mouse embryonic stem cells. *Nucleic Acids Res* **40**, e97 (2012).
22. Wang, W., Bradley, A. & Huang, Y. A piggyBac transposon-based genome-wide library of insertionally mutated Blm-deficient murine ES cells. *Genome Res* **19**, 667-673 (2009).
23. Paruzynski, A. et al. Genome-wide high-throughput integrome analyses by nrLAM-PCR and next-generation sequencing. *Nat Protoc* **5**, 1379-1395 (2010).
24. Meder, V.S., Boeglin, M., de Murcia, G. & Schreiber, V. PARP-1 and PARP-2 interact with nucleophosmin/B23 and accumulate in transcriptionally active nucleoli. *J Cell Sci* **118**, 211-222 (2005).
25. Leitinger, N. & Wesierska-Gadek, J. ADP-ribosylation of nucleolar proteins in HeLa tumor cells. *Journal of Cellular Biochemistry* **52**, 153-158 (1993).
26. Kim, K.M. et al. A new MIF4G domain-containing protein, CTIF, directs nuclear cap-binding protein CBP80/20-dependent translation. *Genes Dev* **23**, 2033-2045 (2009).
27. Guettler, S. et al. Structural basis and sequence rules for substrate recognition by Tankyrase explain the basis for cherubism disease. *Cell* **147**, 1340-1354 (2011).

28. Kim, M.K., Dudognon, C. & Smith, S. Tankyrase 1 regulates centrosome function by controlling CPAP stability. *EMBO Rep* **13**, 724-732 (2012).
29. Kodani, A. et al. Centriolar satellites assemble centrosomal microcephaly proteins to recruit CDK2 and promote centriole duplication. *Elife* **4** (2015).
30. Hori, A. & Toda, T. Regulation of centriolar satellite integrity and its physiology. *Cell Mol Life Sci* **74**, 213-229 (2017).
31. Iaconis, D. et al. The centrosomal OFD1 protein interacts with the translation machinery and regulates the synthesis of specific targets. *Sci Rep* **7**, 1224 (2017).
32. Schmid-Burgk, J.L., Honing, K., Ebert, T.S. & Hornung, V. CRISPaint allows modular base-specific gene tagging using a ligase-4-dependent mechanism. *Nat Commun* **7**, 12338 (2016).
33. Hottiger, M.O. SnapShot: ADP-Ribosylation Signaling. *Mol Cell* **62**, 472 (2016).
34. Poser, I. et al. BAC TransgeneOmics: a high-throughput method for exploration of protein function in mammals. *Nat Methods* **5**, 409-415 (2008).
35. Shyu, Y.J., Liu, H., Deng, X. & Hu, C.D. Identification of new fluorescent protein fragments for bimolecular fluorescence complementation analysis under physiological conditions. *Biotechniques* **40**, 61-66 (2006).
36. Lam, A.J. et al. Improving FRET dynamic range with bright green and red fluorescent proteins. *Nat Methods* **9**, 1005-1012 (2012).
37. Li, H. & Durbin, R. Fast and accurate short read alignment with Burrows-Wheeler transform. *Bioinformatics* **25**, 1754-1760 (2009).
38. Quinlan, A.R. & Hall, I.M. BEDTools: a flexible suite of utilities for comparing genomic features. *Bioinformatics* **26**, 841-842 (2010).

Figure legends

Figure 1. PAR biosensors detect cellular PARylation. (**a**) PAR-binding biosensors derived from APLF and CHFR. The PAR-binding PBZ domains were fused to full-length GFP, generating PAR biosensors PBZ-GFP and CHFR-PBZ-GFP, respectively. When CHFR PBZ biosensor is used it is explicitly annotated; in all other cases the APLF PBZ biosensor is used. (**b**,**c**) PAR-binding biosensor signal correlates with PAR immunodetection but has a greater dynamic range. HeLa cells expressing PBZ-GFP were exposed to 1 mM H_2O_2 or 1 μM olaparib; GFP signal and PAR (10H anti-PAR antibody) were monitored 10 min after exposure. (**b**) Scatter plots of the PAR biosensor intensity correlate with the PAR Ab detection. Intensities were measure in >1000 cells per condition. (**c**) Fold change in median signal in H_2O_2 *vs.* mock, and olaparib *vs.* mock are shown for both PAR detection approaches (exemplary images are shown in Supplementary Fig. 1.A). NS – not significant, box plot shows quartiles, Student's *t*-test ** - *p*-values<0.01. (**d**,**f**) Kinetics of PARylation at sites of DNA damage. *PARP1* null CAL51 cells (CAL51 *PARP1*$^{-/-}$) were transfected with PARP1-GFP and PBZ-mRuby2 and exposed to localized (micro)irradiation as shown in (**d**). After microirradiation, PARP1 and PAR localisation were monitored over time. A microirradiated cell is shown; the area that is shown on the subsequent kymographs is annotated with a white box with a 2 μm side. Scale bar represents 5 μm. (**e**) Kymograph (top) and graph (bottom) of PARP1 and PBZ-mRuby2 0-3 s after microirradiation. (**f**) as per (**e**) but 0-10 minutes after microirradiation. Each graph shows average signals from >10 cells; scale bar represents a distance of 2 μm. (**g**,**h**) A PAR biosensor detects loss of PAR at microirradiated sites caused by PARP1 mutations. (**g**) PARP1 bound to a double strand break (4OQB) with indicated: p.[43delM;44F>I] and E988K mutations in red. (**h**) Kymographs are shown from microirradiated CAL51 *PARP1*$^{-/-}$ cells expressing PBZ-mRuby2 and either wild type PARP1-GFP, PARP1-p.[43delM;44F>I]-GFP, or PARP1-

824 E988K-GFP. (**i**) The clinical PARP inhibitor talazoparib reduces PAR levels at sites of
825 microirradiation. Kymographs of HeLa cells with a PARP1-GFP containing bacterial
826 artificial chromosome (PARP1-LAP) and PBZ-mRuby2 were exposed to 100 nM
827 talazoparib for 1 h prior to microirradiation.
828
829
830 **Figure 2. Bimolecular fluorescent complementation** (**BiFC) PAR biosensors detect**
831 **cellular PARylation.** (**a**) BiFC PAR biosensor - PBZ coding sequence was fused to the
832 N-terminus of Venus (VN) (PBZ-VN); the C-terminus of Venus (VC) was fused to query
833 protein (protein-VC). PARylation of the query protein leads to VC-VN interaction and
834 restoration of a fluorescent GFP. (**b**) HeLa cells were transfected with constructs
835 expressing: VN + VC, PBZ-VN, PBZ-VC, PBZ-VN + PBZ-VC or PBZ-4A-VN + PBZ-4A-
836 VC (4A constructs lack PAR binding). Cells were mock-treated or exposed to 1 mM H_2O_2
837 and stained with PAR-binding reagent (Millipore). GFP nuclear foci are observed only in
838 the PBZ-VN + PBZ-VC, and are marked by PAR-binder staining. (**c**) A quantification of
839 PAR nuclear intensity as shown in (**b**). GFP+ and GFP- represents the PAR intensity of
840 sensor-transfected or not-transfected cells. PBZ-VN + PBZ-VC expression leads to PAR
841 accumulation in the absence of damage. Mean and standard deviations are shown for
842 >20 nuclei. (**d**) Confocal images of *PARP1* wild type or *PARP1*$^{-/-}$ CAL51 cells
843 expressing, PBZ-VN + PBZ-VC or PBZ-4A-VN + PBZ-4A-VC. PBZ-4A. Loss of PARP1
844 or PARP1 inhibition (olaparib) ablated the formation of nuclear GFP foci, whilst the
845 tankyrase inhibitor (ICR-TNKS-001) did not; mean nuclear GFP intensity from >20
846 nuclei; box plot shows quartiles, ** - Student's *t*-test *p*-values<0.01. (**e**) Kinetics of
847 PARylation at microirradiation sites. Kymographs and graphs of the GFP signal in
848 *PARP1* wild type or *PARP1*$^{-/-}$ CAL51 cells with either PBZ-VN + PBZ-VC sensors or
849 PBZ-4A-VN + PBZ-4A-VC sensors. (**f**) The PARP inhibitor talazoparib modulates PAR

foci. HeLa cells, expressing PBZ-VN + PBZ-VC, were exposed to 100 nM talazoparib overnight; the cells were washed in drug-free media and imaged. After removal of talazoaprib, biosensor signal in the cytoplasm (yellow arrow) reduced; whilst the frequency of GFP+ nuclear foci (red arrows) increased. (**g**) PAR Biosensor detects nuclear/cytoplasmic localisation patterns of known PARylated proteins. HeLa cells were co-transfected with PBZ-VN or PBZ-4A-VN plus AXIN-VC, TERF1-VC, TNKS2_800-1161-VC or GLUT4-VC. PBZ-VN transfected cells revealed protein-specific localisation pattern, whilst PBZ-4A-VN transfected cells did not. Scale bars represent 5 μm.

Figure 3. A transposon-based biosensor screen to identify PARylated proteins. (**a**) A genetic screen to identify PARylation events. (i) UPATrap-VC was introduced into CAL51 cells, generating six tagged cell libraries (5000 clones each). (ii) Either PBZ-GF, PBZ-VN or PBZ-4A-VN biosensors were introduced into each library and GFP-positive cells were isolated (iii); PBZ-GFP showed 60% GFP-positive cells, while the PBZ-VN constructs showed 0.1% GFP-positive cells. (iv) Genomic DNA was isolated from GFP-positive cells and UPATrap-VC integration sites identified by non-restrictive linear amplification PCR (nrLAM-PCR) followed by deep sequencing. Each gDNA sample was amplified and sequenced in three independent reactions (A, B, C). (**b**) A schematic of the transposon-mediated VC tagging, when an UPATrap-VC transposon is introduced into genes. Yellow triangles = *Tol2* transposon repeats; SA = splicing acceptor; SD = splicing donor, IRES = internal ribosome entry site, NeoR = G418-resistance gene; pA = polyAdenylation signal. Integration of UPATrap-VC into genes results in the production of protein-VC fusion proteins and NeoR protein. (**c**) Integration of a full-length GFP version of UPATrap (UPATrap-GFP) generates specific localisation pattern in different GFP-positive colonies. This suggests that the transposon has captured and generated in-frame protein-VC fusion in a specific gene. (**d**) nrLAM-PCR and deep sequencing

from independent reactions is highly reproducible. Scatter plots are shown illustrating the correlation between unique read depth from three replica nrLAM-PCR and sequencing reactions (A, B and C); Spearman's rank correlation >0.98. (**e**) Distribution of sequencing depth across all libraries in the screen. Approximately 50 genomic sites were represented by a unique read depth of >30 reads (see detailed description in methods). (**f**) A schematic representation of the three genes identified with two, independent, transposon integration sites (indicated by red circles). (**g**) Biosensor signal obtained by the expression of full-length NPM1-VC and CTIF-VC in combination with PNZ-VN. The cells were co-stained with antibodies, recognizing the endogenous NPM1 and CTIF, respectively. (**h**) PARylation biosensor screen detects "hits" with different subcellular localisation. Confocal imaging of VC-VN GFP signal for 11 genes identified in the screen are shown. NPM1 is a known PARylation target. Scale bars represent 5 μm.

Figure 4. CTIF is PARylated in a TNKS-dependent manner. A schematic of the *CTIF* 3´ end with Tol2 integration sites (red circles) (**a**), nrLAM-PCR products (**b**) and generated CTIF-VC fusion proteins (**c**) identified in the screen. (**d**) CTIF biosensor is localises to the centrosomal area of the cell (white arrowheads). HeLa cells were transfected with CTIF-VC + PBZ-VN or CHFR-PBZ-VN and immunostained with an anti-CTIF antibody. (**e**) CTIF localises with centrosomal markers. HeLa cells were transfected with centrosome markers CETN2-GFP or Cep170-GFP, and co-stained with anti-CTIF antibody. Cells expressing either CTIF-GFP or (CTIF-VC + PBZ-VN) were co-stained with anti-CETN3 or anti-γTubulin. CTIF-GFP is broadly distributed in the cells, while the CTIF biosensor is surrounding the centrosome. White arrowheads indicate the area that is shown in insets with 2 μm side. (**f**) CTIF localises to the daughter centriole. HeLa cells were transfected with CETN2-GFP (marks both centrioles) or Cep170-GFP (marks the mother centriole), and stained with anti-CTIF antibody. (**g**) Tankyrase inhibition reduces

CTIF biosensor signal. HeLa cells, expressing CTIF-VC + PBZ-VN, were exposed to olaparib or ICR-TNKS-001. Quantification of the GFP signal over >20 cells in three independent experiments is shown, NS – not significant, box plot shows quartiles, ** - Student's *t*-test *p*-values<0.01. (**h**) Tankyrase depletion reduces CTIF biosensor signal, as in (**g**) TNKS + TNKS2 siRNA did not reduce CTIF expression (CTIF-GFP). The efficiency of depletion is shown on the Western blot in panel (**i**). (**j**) CTIF is a direct PARylation target. CTIF-GFP was immunoprecipitated with anti-GFP antibody and immunoblotted with anti-PAR (10H) antibody. Uncropped blots are shown in Supplementary Fig. 4.F. (**k**) CTIF has a N-terminal CBP80 (AA 1-305) and a C-terminal MIF4G (AA 380-600) domain. A deletion series was fused to either full-length GFP or VC sequence. CAL51 cells, expressing GFP-fused variants showed broad cytoplasmic distribution, whilst the VC-fused ones showed localized patterns. Centrosome signal was observed with the full length CTIF, and with the N-terminal CBP80 domain, down to the 100 most N-terminal amino acids (white arrows). All constructs were expressed at a similar protein level (Supplementary Fig. 4g). Scale bars represent 5 μm.

Figure 5. CTIF modulates centrosomal satellites. (**a**) CTIF biosensor localises and segregates with the centrosome. Live cell imaging of H2B-cherry HeLa cells expressing either CTIF-GFP or CTIF-VC + PBZ-VN showed that CTIF-GFP is distributed throughout the cytoplasm during M phase (top images), whilst CTIF-VC + PBZ-VN signal (lower images) segregated with the centrosome during mitosis. Detailed time series are shown in Supplementary Fig. 5a. (**b**) CTIF biosensor localisation is microtubule-dependent. HeLa cells expressing CTIF-VC + PBZ-VN were exposed to either nocodazole or paclitaxel. Nocodazole caused a reversible dispersal of the signal whilst the microtubule-stabilising drug paclitaxel did not. (**c**) Schematic illustrating the centrosome with a central pair of centrioles, surrounded by pericentrosomal material (PCM), microtubules (MT) and

centrosomal satellites (CS). (**d**) Co-localisation of CTIF biosensor and various centrosomal markers showed that PARylated CTIF is peripheral to inner centrosomal markers (CETN3 and PCNT) and PCM (PCNT and PCM1), whilst it is localised in the area occupied by the centrosomal satellites (Cep131/Azi1, Cep290 and BBS4); insets are with 2 μm sides. (**e**) CTIF PARylation biosensor co-localises with tankyrase. HeLa cells transfected with CTIF-VC + PBZ-VN were immunostained for endogenous tankyrase; scale bars in the zoomed images represent 1 μm. (**f**) CTIF depletion affects the centrosomal satellites, but not the core centrosome. HeLa cells were depleted by *CTIF* or tankyrase (*TNKS* + *TNKS2*) siRNA and immunostained for various centrosomal markers. Images show staining for the centrosomal satellite marker Cep131/Azi1 and for the core centrosome marker PCNT together with centrosomal marker γTubulin. Images for all the other analyzed markers are shown in Supplementary Fig. 5b and full summary is provided in Table 2. The average intensity of the signal at the centrosomal area was quantified in n = 150 nuclei and normalized to the median of the mock-transfected cells. Box plot shows that CTIF depletion, and to a lower extend tankyrase depletion, leads to the dispersal of the centrosomal satellite (Cep131/Azi1 quantified in (**g**)), whilst not affecting the core centrosome (PCNT quantified in (**h**)); box plot shows quartiles, *p*-values were calculated by two-sided Student's *t*-test. Scale bars represent 5 μm.

Table 1. A summary of the Tol2 integration sites identified in the PARylation screens. The position of the integration, the host gene information, the number of the unique-length reads obtained by the nrLAM-PCR, and the length of the N-terminally truncated fragment for each protein are shown for each insertion site.

Chr	Strand orientation	Insertion site (genomic position)	Median_read_sample	Nr Insertion sites	Gene	Gene ID	Truncation (N-terminal AA)	Protein length (AA)
5	+	170827447	502	2	NPM1	ENSG00000181163	195	259
5	+	170823418	321	2	NPM1	ENSG00000181163	174	259
18	+	46304668	1131	2	CTIF	ENSG00000134030	459	600
18	+	46366092	777	2	CTIF	ENSG00000134030	551	600
9	+	15888921	471	2	CCDC171	ENSG00000164989	1200	1326
9	+	15887412	361	2	CCDC171	ENSG00000164989	1200	1326
1	+	95306653	972	1	SLC44A3	ENSG00000143036	253	653
8	-	119229899	612	1	SAMD12	ENSG00000177570	155	161
6	+	25600895	572	1	LRRC16A	ENSG00000079691	1039	1371
5	-	76998018	420	1	TBCA	ENSG00000171530	55	108
19	+	39122699	377.5	1	EIF3K	ENSG00000178982	119	218
3	-	30786048	376	1	GADL1	ENSG00000144644	464	521
19	-	40368616	339.5	1	FCGBP	ENSG00000090920	4157	5405

9	+	130443026	313.5	1	STXBP1	ENSG00000136854	515	594
3	+	142745673	166	1	U2SURP	ENSG00000163714	426	1029
19	+	10797868	144	1	ILF3	ENSG00000129351	690	702
2	-	45729067	80	1	SRBD1	ENSG00000068784	624	995
3	+	29904702	43.5	1	RBMS3	ENSG00000144642	212	433
3	+	155641886	38	1	GMPS	ENSG00000163655	478	693
4	+	71665115	22	1	RUFY3	ENSG00000018189	520	620

Table 2. A summary of the CTIF and tankyrase (TNKS + TNKS2) depletion phenotypes on various centrosomal markers. Various centrosomal markers were immunodetected (as in Fig.Fig. 5d) after RNAi-mediated depletion of either CTIF, or TNKS + TNKS2 in either HeLa, or CAL51 cells. "**+**" denotes localisation similar control depleted cells, "**+/-**" denotes diminished centrosomal localisation, "**-**" denotes absent or severely diminished centrosomal localisation.

Marker protein	CETN3	PCNT	PCM1	BBS4	Cep290	Cep131 Azi1	OFD1	TNKS TNKS2	CTIF-VC WT-VN
Localisation	Centrioles	Centrioles PCM	PCM CS	CS	CS	CS	CS		
RNAi									
siCon	**+**	**+**	**+**	**+**	**+**	**+**	**+**	**+**	**+**
siTNKS + siTNKS2	**+**	**+**	**+**	**+/-**	**+/-**	**+/-**	**+**	**-**	**-**
siCTIF	**+**	**+**	**+**	**-**	**-**	**-**	**+**	**+**	**-**

Figure 1

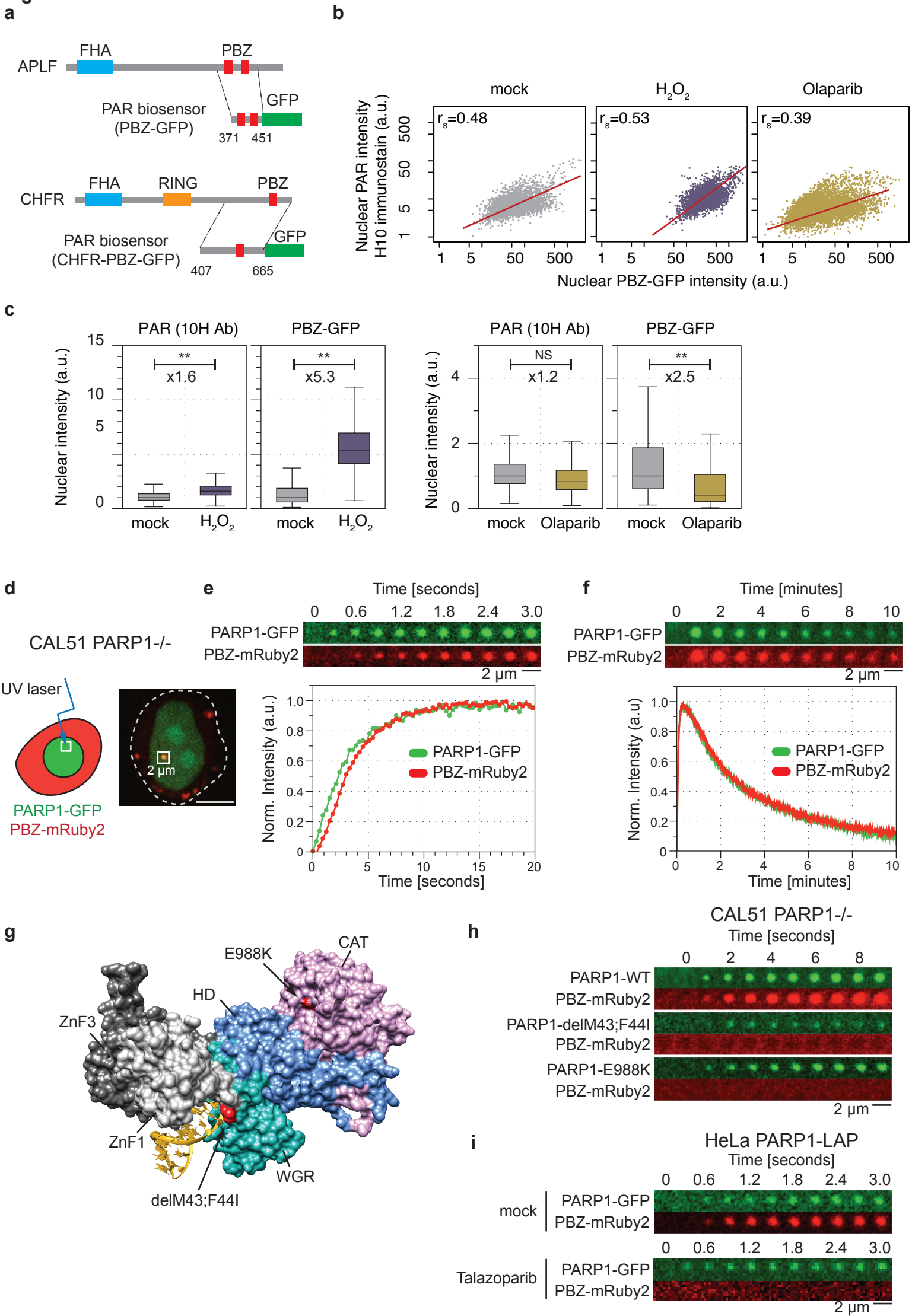
a
FHA
PBZ
APLF
GFP
PAR biosensor
(PBZ-GFP)
371
451
FHA
RING
PBZ
CHFR
GFP
PAR biosensor
(CHFR-PBZ-GFP)
407
665
b
mock
H2O2
Olaparib
Nuclear PAR intensity
H10 immunostain (a.u.)
rs=0.48
rs=0.53
rs=0.39
Nuclear PBZ-GFP intensity (a.u.)
c
PAR (10H Ab)
PBZ-GFP
Nuclear intensity (a.u.)
x1.6
x5.3
NS
x1.2
x2.5
mock
H2O2
Olaparib
d
CAL51 PARP1-/-
UV laser
PARP1-GFP
PBZ-mRuby2
2 µm
e
Time [seconds]
PARP1-GFP
PBZ-mRuby2
2 µm
Norm. Intensity (a.u.)
f
Time [minutes]
g
CAT
E988K
HD
ZnF3
ZnF1
WGR
delM43;F44I
h
CAL51 PARP1-/-
Time [seconds]
PARP1-WT
PBZ-mRuby2
PARP1-delM43;F44I
PARP1-E988K
i
HeLa PARP1-LAP
Time [seconds]
mock
Talazoparib

Figure 2

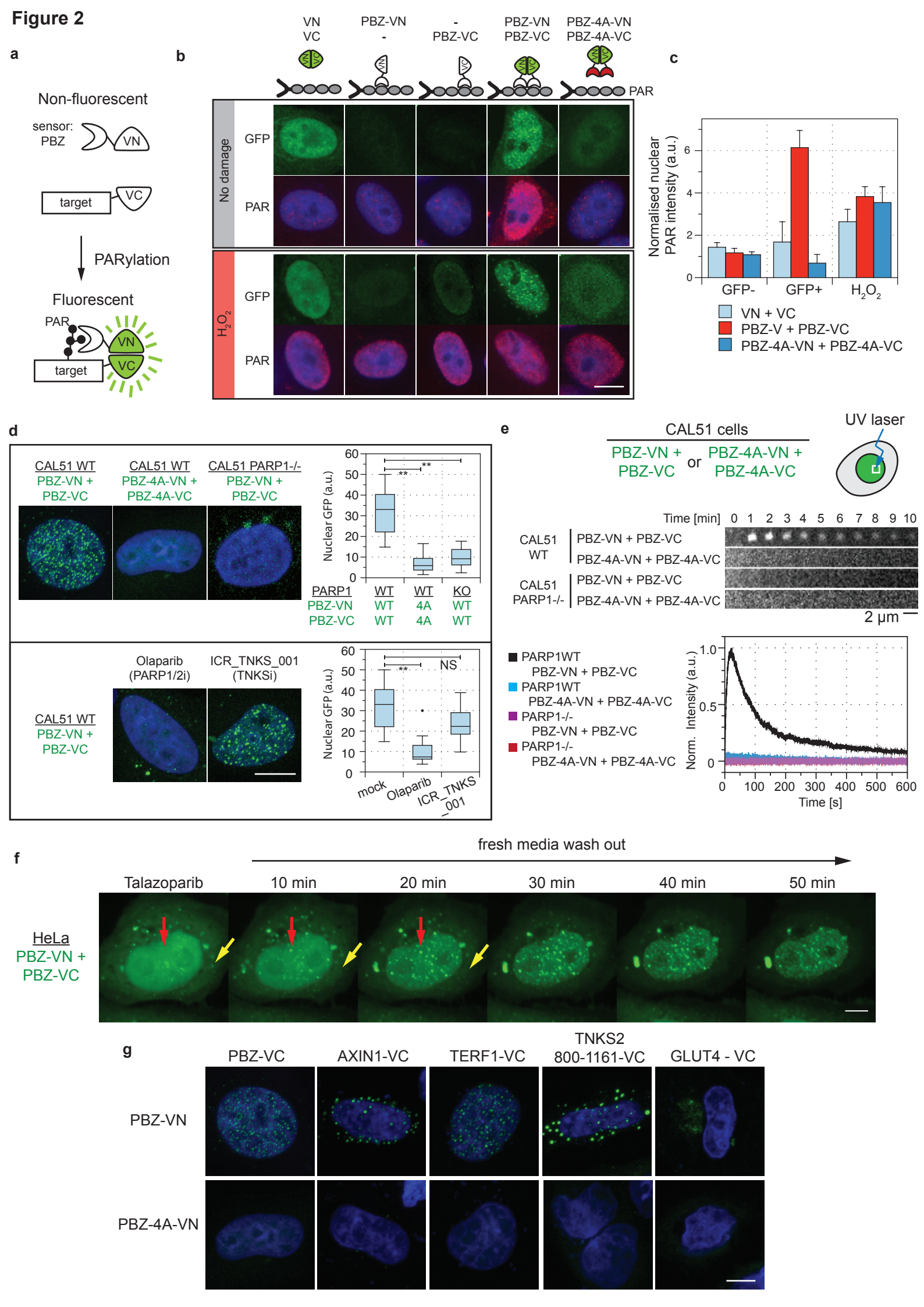
a
Non-fluorescent
sensor: PBZ
VN
target
VC
PARylation
Fluorescent
PAR
VN
VC
target
b
VN
VC
PBZ-VN
-
-
PBZ-VC
PBZ-VN
PBZ-VC
PBZ-4A-VN
PBZ-4A-VC
PAR
No damage
GFP
PAR
H2O2
GFP
PAR
c
Normalised nuclear PAR intensity (a.u.)
0
2
4
6
GFP-
GFP+
H2O2
VN + VC
PBZ-V + PBZ-VC
PBZ-4A-VN + PBZ-4A-VC
d
CAL51 WT
PBZ-VN +
PBZ-VC
CAL51 WT
PBZ-4A-VN +
PBZ-4A-VC
CAL51 PARP1-/-
PBZ-VN +
PBZ-VC
Nuclear GFP (a.u.)
0
10
20
30
40
50
60
**
**
PARP1
PBZ-VN
PBZ-VC
WT
WT
WT
WT
4A
4A
KO
WT
WT
CAL51 WT
PBZ-VN +
PBZ-VC
Olaparib
(PARP1/2i)
ICR_TNKS_001
(TNKSi)
Nuclear GFP (a.u.)
0
10
20
30
40
50
60
**
NS
mock
Olaparib
ICR_TNKS_001
e
CAL51 cells
PBZ-VN + PBZ-VC
or
PBZ-4A-VN + PBZ-4A-VC
UV laser
Time [min]
0 1 2 3 4 5 6 7 8 9 10
CAL51 WT
PBZ-VN + PBZ-VC
PBZ-4A-VN + PBZ-4A-VC
CAL51 PARP1-/-
PBZ-VN + PBZ-VC
PBZ-4A-VN + PBZ-4A-VC
2 µm
PARP1WT
PBZ-VN + PBZ-VC
PARP1WT
PBZ-4A-VN + PBZ-4A-VC
PARP1-/-
PBZ-VN + PBZ-VC
PARP1-/-
PBZ-4A-VN + PBZ-4A-VC
Norm. Intensity (a.u.)
0
0.5
1.0
0
100
200
300
400
500
600
Time [s]
f
fresh media wash out
Talazoparib
10 min
20 min
30 min
40 min
50 min
HeLa
PBZ-VN +
PBZ-VC
g
PBZ-VC
AXIN1-VC
TERF1-VC
TNKS2
800-1161-VC
GLUT4 - VC
PBZ-VN
PBZ-4A-VN

Figure 3

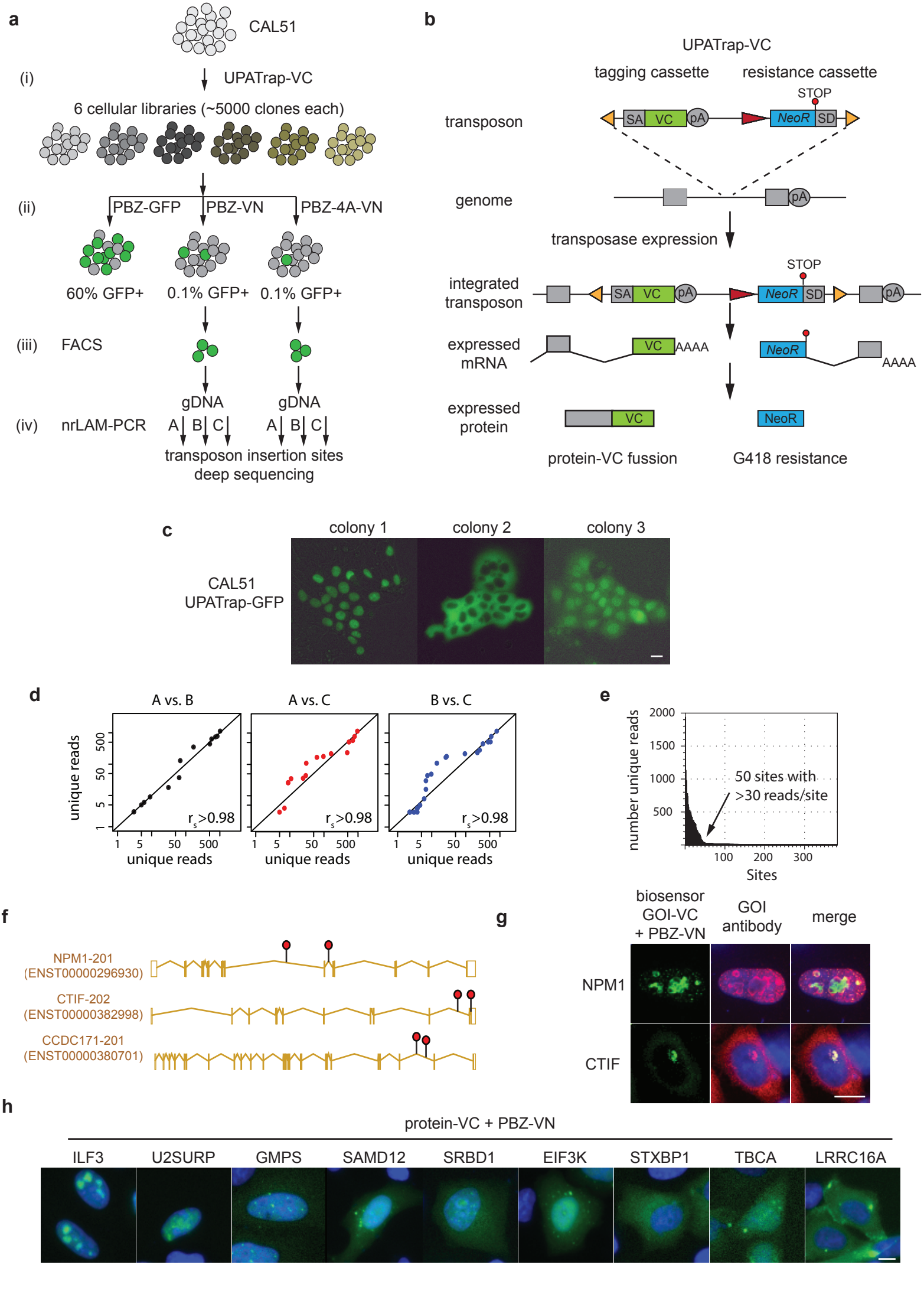
a
CAL51
(i)
UPATrap-VC
6 cellular libraries (~5000 clones each)
(ii)
PBZ-GFP
PBZ-VN
PBZ-4A-VN
60% GFP+
0.1% GFP+
0.1% GFP+
(iii)
FACS
gDNA
gDNA
(iv)
nrLAM-PCR
A B C
A B C
transposon insertion sites
deep sequencing
b
UPATrap-VC
tagging cassette
resistance cassette
STOP
transposon
SA
VC
pA
NeoR
SD
genome
pA
transposase expression
STOP
integrated transposon
expressed mRNA
AAAA
AAAA
expressed protein
protein-VC fussion
G418 resistance
c
colony 1
colony 2
colony 3
CAL51
UPATrap-GFP
d
A vs. B
A vs. C
B vs. C
unique reads
r_s>0.98
e
number unique reads
50 sites with
>30 reads/site
Sites
f
NPM1-201
(ENST00000296930)
CTIF-202
(ENST00000382998)
CCDC171-201
(ENST00000380701)
g
biosensor
GOI-VC
+ PBZ-VN
GOI
antibody
merge
NPM1
CTIF
h
protein-VC + PBZ-VN
ILF3
U2SURP
GMPS
SAMD12
SRBD1
EIF3K
STXBP1
TBCA
LRRC16A

Figure 4

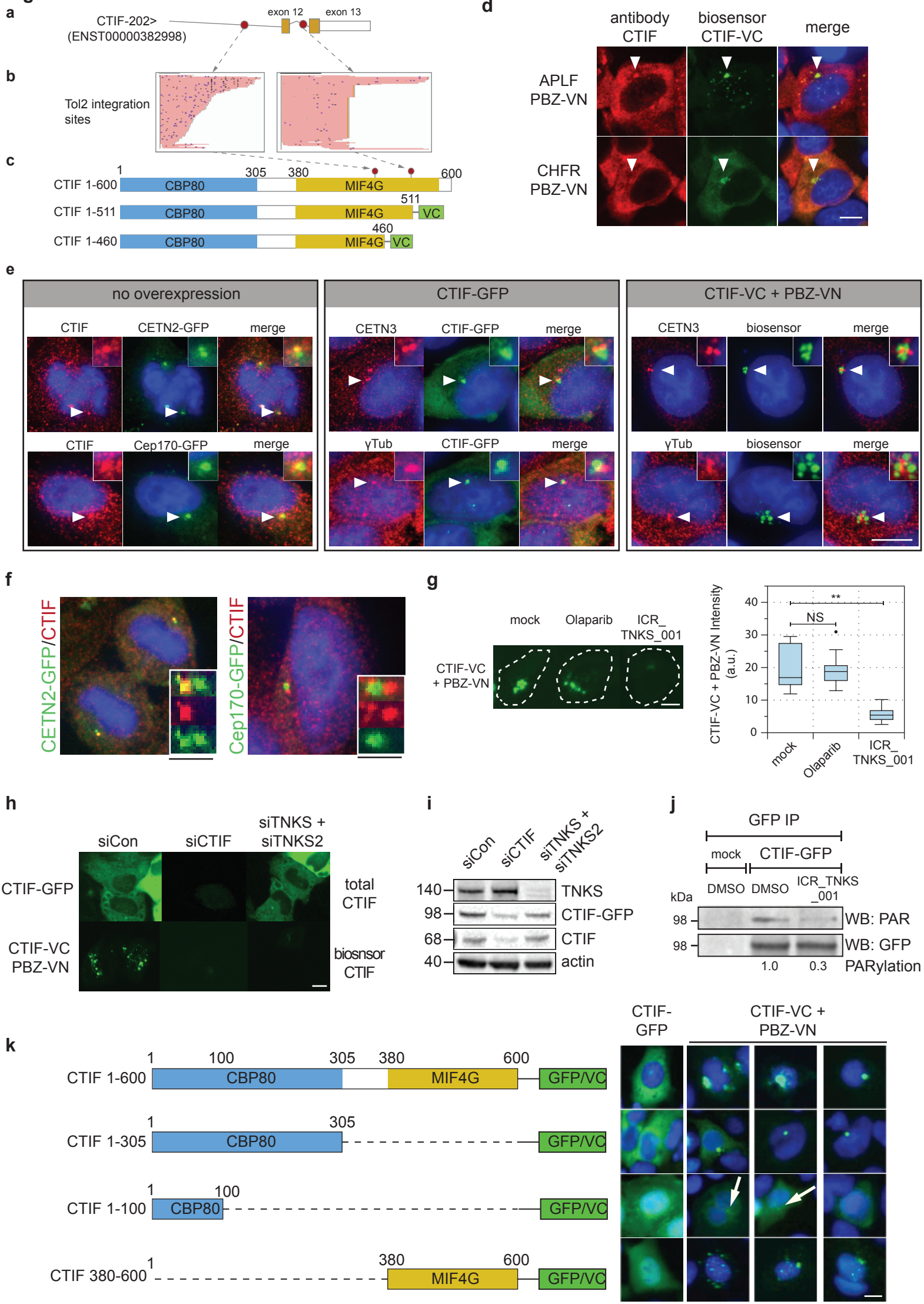
a
CTIF-202>
(ENST00000382998)
exon 12
exon 13
b
Tol2 integration
sites
c
1
305
380
600
CTIF 1-600
CBP80
MIF4G
511
CTIF 1-511
CBP80
MIF4G
VC
460
CTIF 1-460
CBP80
MIF4G
VC
d
antibody
CTIF
biosensor
CTIF-VC
merge
APLF
PBZ-VN
CHFR
PBZ-VN
e
no overexpression
CTIF-GFP
CTIF-VC + PBZ-VN
CTIF
CETN2-GFP
merge
CETN3
CTIF-GFP
merge
CETN3
biosensor
merge
CTIF
Cep170-GFP
merge
γTub
CTIF-GFP
merge
γTub
biosensor
merge
f
CETN2-GFP/CTIF
Cep170-GFP/CTIF
g
mock
Olaparib
ICR_
TNKS_001
CTIF-VC
+ PBZ-VN
CTIF-VC + PBZ-VN Intensity
(a.u.)
40
30
20
10
0
**
NS
mock
Olaparib
ICR_
TNKS_001
h
siCon
siCTIF
siTNKS +
siTNKS2
CTIF-GFP
CTIF-VC
PBZ-VN
total
CTIF
biosnsor
CTIF
i
siCon
siCTIF
siTNKS +
siTNKS2
140
98
68
40
TNKS
CTIF-GFP
CTIF
actin
j
GFP IP
mock
CTIF-GFP
DMSO
DMSO
ICR_TNKS
_001
kDa
98
98
WB: PAR
WB: GFP
1.0
0.3
PARylation
k
CTIF 1-600
CBP80
MIF4G
GFP/VC
CTIF 1-305
CBP80
GFP/VC
CTIF 1-100
CBP80
GFP/VC
CTIF 380-600
MIF4G
GFP/VC
1
100
305
380
600
CTIF-
GFP
CTIF-VC +
PBZ-VN

Figure 5

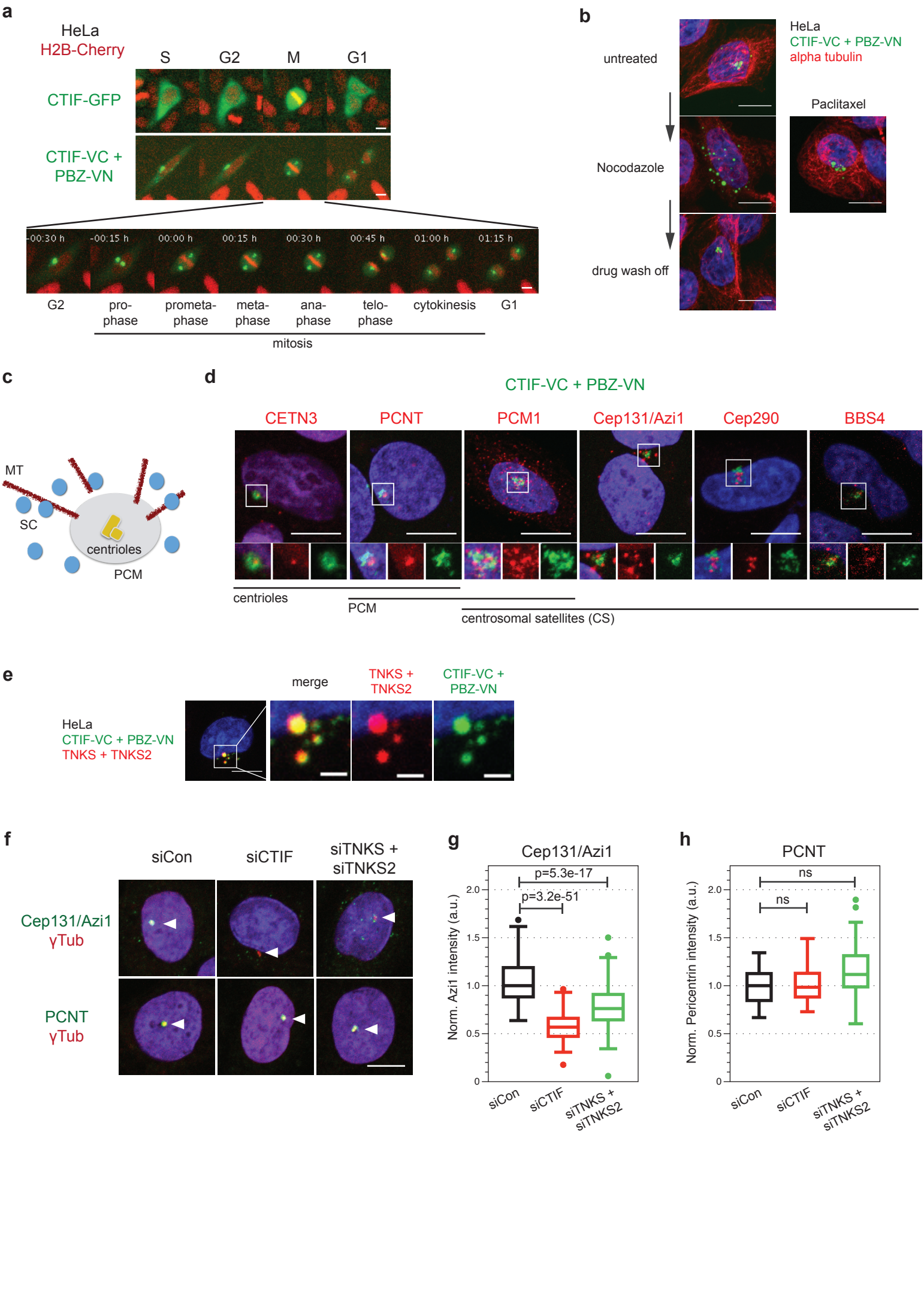
a
HeLa
H2B-Cherry
S
G2
M
G1
CTIF-GFP
CTIF-VC +
PBZ-VN
-00:30 h
-00:15 h
00:00 h
00:15 h
00:30 h
00:45 h
01:00 h
01:15 h
G2
pro-
phase
prometa-
phase
meta-
phase
ana-
phase
telo-
phase
cytokinesis
G1
mitosis
b
untreated
Nocodazole
drug wash off
HeLa
CTIF-VC + PBZ-VN
alpha tubulin
Paclitaxel
c
MT
SC
centrioles
PCM
d
CTIF-VC + PBZ-VN
CETN3
PCNT
PCM1
Cep131/Azi1
Cep290
BBS4
centrioles
PCM
centrosomal satellites (CS)
e
HeLa
CTIF-VC + PBZ-VN
TNKS + TNKS2
merge
TNKS +
TNKS2
CTIF-VC +
PBZ-VN
f
siCon
siCTIF
siTNKS +
siTNKS2
Cep131/Azi1
γTub
PCNT
γTub
g
Cep131/Azi1
p=5.3e-17
p=3.2e-51
Norm. Azi1 intensity (a.u.)
2.0
1.5
1.0
0.5
0
siCon
siCTIF
siTNKS +
siTNKS2
h
PCNT
ns
ns
Norm. Pericentrin intensity (a.u.)
2.0
1.5
1.0
0.5
0
siCon
siCTIF
siTNKS +
siTNKS2